Journal of Materials Chemistry C

ROYAL SOCIETY OF CHEMISTRY

PAPER

View Article Online
View Journal

Cite this: DOI: 10.1039/d5tc03535j

Hysteresis-encoded thermometry in the cryogenic regime using a Dy-single-molecule magnet

Shraoshee Shome and Sanjit Konar *

Received 26th September 2025,
Accepted 19th December 2025

DOI: 10.1039/d5tc03535j

rsc.li/materials-c

Precise cryogenic thermometry (<10 K) in single-molecule magnets (SMMs) remains a critical challenge, as conventional approaches often suffer from poor sensitivity and limited applicability. To address this, we present a hysteresis-based thermometry approach with a Dy(III)-SMM, which leverages key magnetic parameters from hysteresis loops to provide a sensitive alternative. Three distinct hysteresis parameters – saturation magnetisation (M_S), remanent magnetisation (M_R), and loop area (A) – have been used in the 2–8 K regime for thermometry. All three parameters decrease monotonically with increasing temperature, and this temperature dependence results in excellent relative thermal sensitivities (S_r), following the trend $S_r^A > S_r^R > S_r^S$. Furthermore, scan rate-dependent analyses have been performed, showing negligible variations across different sweep rates, confirming the stability of the thermometric response under varying scan conditions. This work represents the first demonstration of hysteresis-based thermometry in SMMs, providing a versatile route for cryogenic sensing by utilising the intrinsic magnetisation dynamics, with promising implications for quantum and low-temperature device applications.

Introduction

Single-molecule magnets (SMMs) have emerged as promising candidates for next-generation quantum technologies, including quantum information processing, molecular spintronics, and high-density data storage.[1–8] Their unique ability to retain magnetisation at the molecular level, coupled with tunable magnetic relaxation dynamics, makes them attractive building blocks for nanoscale devices.[9–16] However, most of the SMMs operate intrinsically in the cryogenic regime, where spin relaxation is sufficiently slow to sustain the quantum coherence.[17–20] Precise thermometry below 10 K is particularly important in this regard as (i) in this region, small thermal fluctuations can strongly influence magnetic relaxation pathways, quantum tunnelling rates, and spin–phonon interactions,[1] critically affecting the physical behaviour of SMMs; (ii) from a technological perspective, accurate sub-10 K temperature readout is essential for calibration and reliable operation of cryogenic quantum devices and low-temperature magnetic memory systems.[21–23] Traditional approaches to temperature sensing in SMMs have relied mostly on luminescence thermometry (based on emission band shift, lifetime, intensity, *etc.*).[24–42] Recently, magneto-thermometry using relaxation time (τ), magnetic susceptibility (χ),[43] magneto-chiral dichroism (MCD),[17] and magnetic circularly polarised luminescence (MCPL)[44] has also been reported. While these methods have been successful at moderate cryogenic as well as high temperatures, their sensitivity and reliability often deteriorate below 10 K. For example, below 10 K, luminescence thermometry faces challenges due to reduced Boltzmann redistribution,[45] magneto-thermometry using $1/\chi$ fails below 10 K due to deviation from Curie behaviour (<10 K magnetic anisotropy dominates), and magneto-thermometry using τ fails due to the dominance of temperature-independent relaxation, such as quantum tunnelling of magnetisation (QTM).[43] MCD-based thermometry has a strong dependence on transmission geometry and magnetic field stability, making real-life implementation technically challenging, and it is further restricted to SMMs that exhibit MCD, thereby narrowing its applicability.[17] Thus, there is a pressing need for innovative thermometry strategies specifically tailored to the deep-cryogenic (sub-10 K) regime, which can provide an intrinsic, reliable, and sensitive readout of temperature without the limitations of existing methods.

Herein, we introduce a hysteresis-based thermometry strategy that exploits the intrinsic temperature dependence of magnetic hysteresis loop characteristics as thermal markers. For this purpose, we employed the air-stable SMM Dy(BBPEN)Cl[46] (H_2BBPEN = *N*,*N*′-bis(2-hydroxybenzyl)-*N*,*N*′-(2-pyridylmethyl)ethylenediamine, complex **1**; Fig. 1). Complex **1** shows a U_{eff} of 708 K and is particularly suited for such studies owing to its chemical stability (air- and moisture-stable) and the presence of well-defined, pronounced hysteresis loops up to 8 K, as previously reported by Tong and co-workers.[46] Parameters such as saturation magnetisation (M_S), remanent magnetisation (M_R), and loop area (A) extracted

Department of Chemistry, Indian Institute of Science Education and Research Bhopal, Bhopal Bypass Road, Bhauri, Madhya Pradesh, 462066, India. E-mail: skonar@iiserb.ac.in

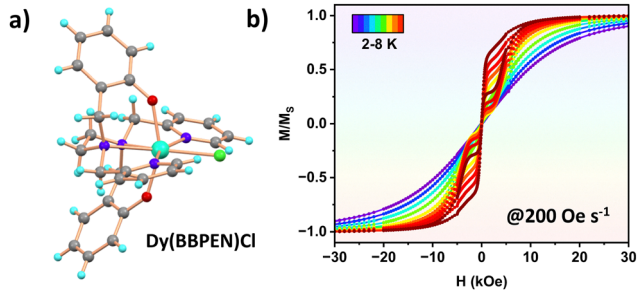

Fig. 1 (a) The molecular structure of complex **1** and (b) variable temperature hysteresis in the 2–8 K temperature range (200 Oe s^{-1}) (colour code: Dy – cyan, C – grey, N – blue, O – red, Cl – green, H – light blue).

from the hysteresis data have a strong possibility of showing temperature dependence, as faster magnetic relaxation at elevated temperatures progressively diminishes their values.[47] This strategy is conceptually straightforward and directly correlates with the slow relaxation dynamics that define SMM behaviour. However, it is not intended to replace luminescence thermometry, which remains simpler and more sensitive whenever strong optical signals and optical access are available, particularly above ~10 K. The value of the present approach lies in situations where optical readout is impractical, such as non-emissive or quenched complexes, or cryogenic device environments where optical access and direct thermometry are difficult. We have used SQUID here solely as a stable calibration platform; the concept can be transferred to miniaturised magnetic sensors (micro-Hall probes, nanoSQUIDs, and magneto-optical or NV-based readouts) in the future. The main limitations lie in the inherent collapse of hysteresis above the blocking temperature and the need for consistent sweep protocols. Thus, this method should be viewed as a complementary, cryogenic-range thermometric tool rather than a universal alternative to optical approaches (details in the SI, Section S6). Since hysteresis properties can be influenced by the magnetic field scan rate, we carried out a systematic scan rate-dependent study to assess the robustness of the method. The analysis shows that although the parameters exhibit minor scan-rate dependence, they follow the same trend and can be reliably employed for thermometry when the scan rate is kept constant. At all scan rates, we observed remanent magnetisation and loop area providing superior sensitivity compared to saturation magnetisation. This proof-of-concept study highlights hysteresis-based thermometry as a promising novel strategy for cryogenic sensing in SMMs.

Results and discussion

Complex **1** was synthesised following the reported literature procedure[46] and characterised by single-crystal X-ray diffraction (SC-XRD), IR spectroscopy (Fig. S1, SI), powder XRD (Fig. S2, SI), and thermogravimetric analysis (TGA; Fig. S3, SI). The hysteresis data were recorded at a 200 Oe s^{-1} scan rate for complex **1**. The magnetic hysteresis loops (Fig. 1 and Fig. S4, SI) remain open at zero field up to 8 K. The corresponding thermometry parameters, such as saturation magnetisation (M_S), remanent magnetisation (M_R), and loop area (A), were extracted from the hysteresis data (details in the SI).[47] M_S and A showed a monotonic decrease with an increase in temperature (T) from 2 to 8 K (Fig. 2 and Fig. S5, SI). This reduction occurs because higher temperatures accelerate magnetic relaxation processes, allowing the spins to realign more rapidly with the applied magnetic field, resulting in a smaller saturation value and an enclosed area.[47] However, in the case of M_R, a shallow maximum is observed around 2.5 K (M_R at 2.5 K exceeds that at 2.0 K, after which it decreases monotonically with temperature; Fig. S5, SI). This low-T dip might be attributed to efficient zero-field QTM at 2.0 K.[48] A slight increase in temperature reduces the exact resonance condition at $H \approx 0$, yielding higher M_R at 2.5 K. Above 2.5 K, M_R further decreases as thermally assisted relaxation starts to dominate at higher T (Fig. S5a, SI). For calibrating the temperature dependence of the thermometry parameters, we employed eqn (1) (Tables S1–S3, SI):

$$A = A_2 + \frac{A_1 - A_2}{1 + \exp\left(\frac{T - T_0}{dT}\right)} \quad (1)$$

where A_1 and A_2 are the values of thermometry parameters at low and high temperatures, respectively; T_0 is the midpoint temperature at which the transition occurs; and dT is the width of the transition (representing steepness). For saturation magnetisation (M_S), the entire 2–8 K temperature range was used for fitting. In contrast, for remanent magnetisation (M_R) and hysteresis loop area (A), the fitting was restricted to the ranges of 2.5–7 K and 2–6 K, respectively (Fig. 2 and Fig. S5, SI). This

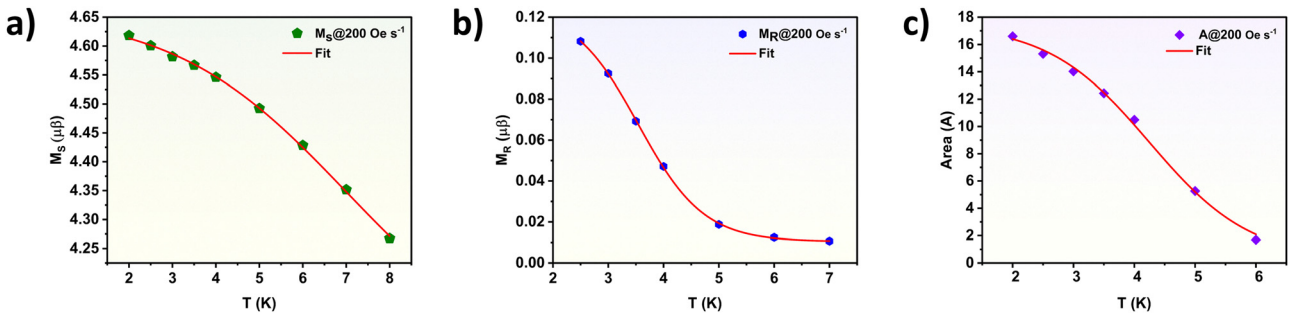

Fig. 2 The temperature dependence of the thermometry parameters: (a) saturation magnetisation, (b) remanent magnetisation, and (c) area fitted to eqn (1) in OriginPro.

restriction was necessary because, outside these temperature windows, the parameter values drop to below ~10% of their maximum, rendering the signal comparable to the experimental noise and thereby leading to unstable and non-reproducible fits. The relative thermal sensitivity (S_r) and temperature uncertainty (δ_T) were calculated using eqn (S1) and (S2) in the SI. The temperature-dependent hysteresis-based parameters reveal distinct thermometry behaviour. For saturation magnetisation, the relative sensitivity (S_r^S) initially increases with temperature, attaining a maximum of 1.8% K^{-1} at 7.14 K, before gradually decreasing at higher temperatures (Fig. 3a). Importantly, S_r^S remains above the 1% K^{-1} threshold throughout the 3.92–8 K range, confirming its reliability in this temperature window. A comparable trend is observed for the remanent magnetisation-based sensitivity (S_r^R), which reaches a maximum of 93.6% K^{-1} at 4.2 K (Fig. 3b) with $S_r^R > 1\%\ K^{-1}$ across the entire 2.5–7 K range, underscoring its robustness as a thermometry parameter. In contrast, the loop area-derived sensitivity exhibits a monotonic increase from 2 to 6 K, peaking with 96.4% K^{-1} at 6 K (Fig. 3c). Throughout this interval, S_r^A continuously remains above 1% K^{-1}, making the loop area a highly effective parameter for precise thermometry.

Overall, these results show that while saturation magnetisation provides moderate sensitivity across a broad temperature range, the loop area uniquely combines high sensitivity with wide applicability, making it the most versatile parameter for practical thermometry. Across all three approaches, the temperature uncertainty remained below 0.1 K, highlighting the accuracy of the hysteresis-based thermometry. From the overall analysis, a clear trend in thermal sensitivity is observed: loop area (S_r^A) > remanent magnetisation (S_r^R) > saturation magnetisation (S_r^S). This hierarchy can be understood by considering how much each parameter reflects the magnetisation changes. The loop area, as an integrated measure of the full hysteresis cycle, exhibits the highest sensitivity since thermal activation simultaneously modulates multiple magnetisation features. In contrast, remanent magnetisation reflects only the zero-field point, capturing a narrower thermal response. Saturation magnetisation is least sensitive, as strong fields align most spins, leaving thermal fluctuations with only a minor influence on the net magnetisation and thus the smallest relative temperature dependence. To check the applicability of our approach to other classes of SMMs, we synthesised $[Dy(L_{phen}^{N6})(Ph_3SiO)_2](PF_6)$ (complex **2**), as reported by Armenis *et al.*[49] The hysteresis-based thermometry for complex **2** yielded an S_{max}^S of 1.1% K^{-1} (at 4.3 K) and an S_{max}^R of 31% K^{-1} (at 3.6 K) (details in the SI, Fig. S9 and S10).

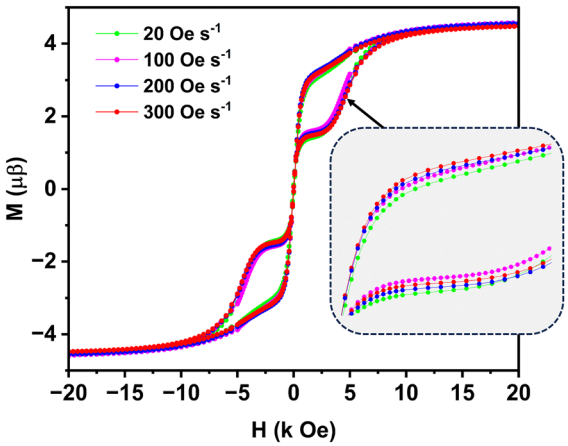

Fig. 4 Variable scan rate hysteresis data of complex **1** at 2 K. The inset shows that a slower scan rate yields a smaller loop compared to a faster scan rate.

To further establish the broader applicability of hysteresis-based thermometry, we conducted scan-rate-dependent studies (20/100/200/300 Oe s^{-1}) on complex **1** (Fig. 4 and Fig. S4, SI). Such an analysis is necessary because all these thermometry parameters are intrinsically governed by magnetic relaxation dynamics, and their quantitative values can vary depending on the applied scan rate. By systematically varying the scan rate, we can assess whether (a) the thermometry parameters exhibit consistent trends, (b) the hierarchy ($S_r^A > S_r^R > S_r^S$) is preserved across all scan rates, and (c) the approach remains valid under different measurement conditions. Together, these evaluations will provide a measure of the approach's overall robustness.

All three parameters exhibit comparable temperature-dependent trends for complex **1**, with only modest changes in their absolute values (Fig. 5 and Fig. S6–S8, SI). For saturation magnetisation (M_s), no difference is observed between 20, 100 and 200 Oe s^{-1}, indicating that Dy^{3+} moments fully align before significant relaxation occurs (Fig. 5a). This points to a scan-rate threshold below which the process remains quasi-equilibrated.

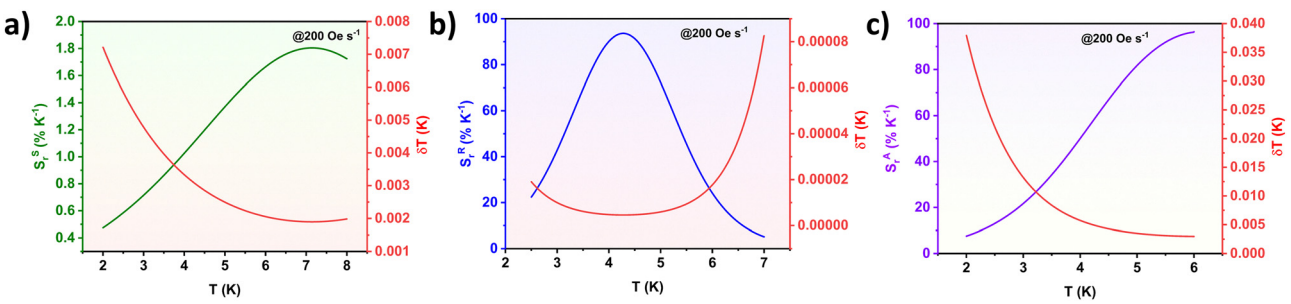

Fig. 3 The temperature dependence of the relative thermal sensitivity and temperature uncertainty in complex **1** corresponding to (a) saturation magnetisation, (b) remanent magnetisation, and (c) loop area.

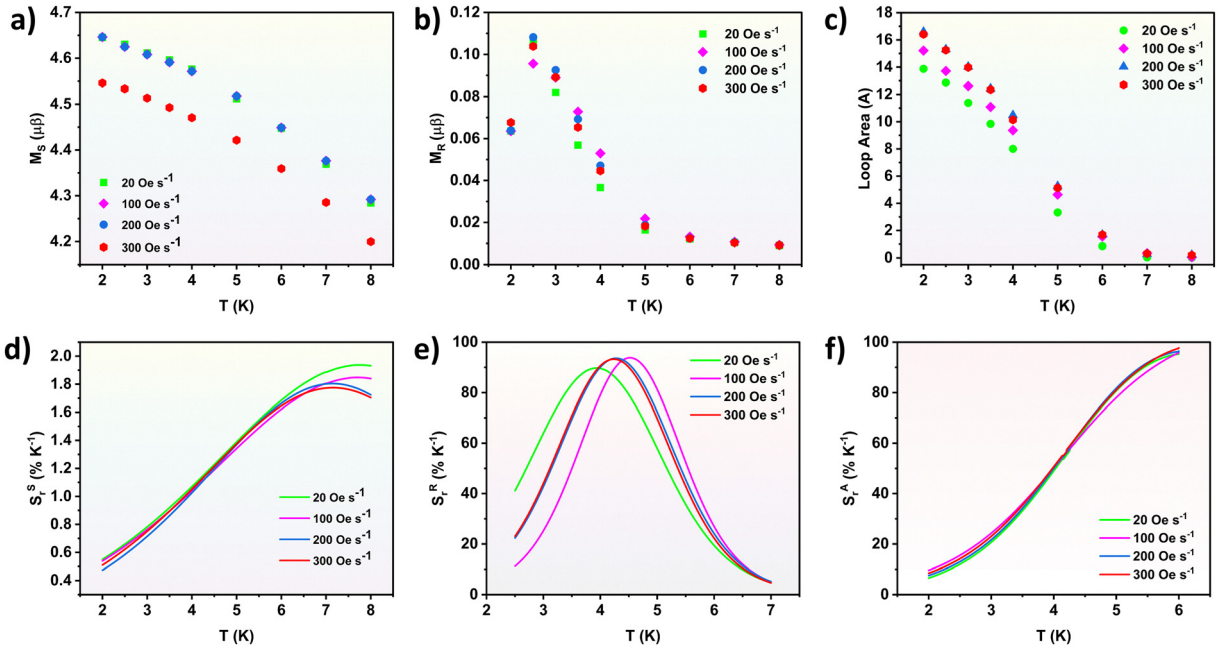

Fig. 5 (a)–(c) Scan rate dependence of the thermometry parameters. (d)–(f) The temperature dependence of the relative thermal sensitivity under different scan rates (scan rates: 20, 100, 200, and 300 Oe s^{-1}).

At higher rates (*e.g.*, 300 Oe s^{-1}), the field change outpaces spin alignment, causing a slight reduction in M_s. Remanent magnetisation (M_r) shows only minor, non-systematic variations at scan rates in the range of 20–300 Oe s^{-1}, with modest scattering at 2–4 K (Fig. 5b). In contrast, the loop area is moderately scan-rate dependent (Fig. 5c), where slower sweeps (20 and 100 Oe s^{-1}) allow greater relaxation and yield narrower loops, whereas faster sweeps (200 and 300 Oe s^{-1}) produce broader loops with a larger area.[50] To assess the reliability of the approach, we compared S_r as a function of temperature at different scan rates (Table S4 and Fig. 5). All parameters show consistent profiles, confirming that the response is intrinsic to relaxation dynamics. Among them, the loop area is the most reproducible, with negligible scan-rate dependence, establishing it as the most reliable metric for cryogenic thermometry. The reported sensitivities for complex **1** are competitive with, and in some cases superior to, those reported for luminescence, MCD-based, and MCPL-based thermometry, highlighting the efficiency of hysteresis-loop features for cryogenic sensing (Table 1 and Fig. S5, SI).

Conclusions

This study presents a proof of concept showing that hysteresis-loop characteristics can act as intrinsic markers for thermometry in Dy-based SMMs. It reduces the need for modification of molecular design by incorporating other complicated properties, such as MCD or luminescence, in SMMs. By systematically analysing the relative sensitivities of saturation magnetisation, remanent magnetisation, and loop area, we obtained excellent magnetothermal sensitivities in the 2–8 K cryogenic range. Validating their applicability across different scan rates, we establish the loop area as the most reliable parameter for thermal readout. These findings provide new insight into the relaxation-governed thermal response of the system, while highlighting hysteresis-derived observables as a promising route for integrating molecular magnetism with precision low-temperature sensing. Looking forward, this approach could be relevant for device applications, such as calibration in dilution refrigerators or on-chip cryogenic temperature sensors.

Table 1 List of single-molecule magnets showing thermometry below 10 K

Formulae	S_{max} (T_{max})	T range (S_r > 1% K^{-1})	Thermometry technique used	Ref.
$[Dy_2(bpm)(tfaa)_6]$	1.8 (5.4)	5.4–85.5	Luminescence	30
$\{[Ho^{III}(4\text{- pyridone})_4(H_2O)_2]$ $[Co(CN)_6]\}\cdot nH_2O$	6.9 (40)	2–140	Luminescence	51
$\{Tb^{III}[Co^{III}(CN)_6]\}$	5.28 (16)	6–92	Luminescence	42
$[Ho(acac)_3(phen)]$	95.3 (2.54)	1.55–5	Magnetic circular dichroism (MCD)	44
[Dy(bbpen)Cl]	1.9 (7.7) from M_S 93.8 (4.5) from M_R 97.7 (6) from A	3.7–8 2.5–7 2–6	Hysteresis-based magneto-thermometry	This work

Author contributions

S. K. and S. S. conceived the idea of the project. S. S. performed all the experiments and analyses and wrote the manuscript with the help of S. K.

Conflicts of interest

There are no conflicts to declare.

Data availability

The data supporting this article have been included as part of the supplementary information (SI). Supplementary information: experimental details, PXRD patterns, FT-IR spectra, TGA data, and additional measurement information. See DOI: https://doi.org/10.1039/d5tc03535j.

Acknowledgements

S. K. thanks the MoE, STARS Grant (Project No. MoE-STARS/STARS-2/2023-0301) for funding and IISER Bhopal for the instrumentation facility. S. S. thanks the PMRF for the research fellowship.

References

1 P.-Y. Liao, H.-R. Xing, Y.-L. Zhong, X.-N. Xu, P.-X. Lu, S.-D. Jiang, C.-H. Li, J.-L. Liu, R. A. Layfield and M.-L. Tong, *J. Am. Chem. Soc.*, 2025, **147**, 22714–22724.
2 C.-J. Yu, S. von Kugelgen, D. W. Laorenza and D. E. Freedman, *ACS Cent. Sci.*, 2021, **7**, 712–723.
3 X.-F. Ma, D. Zeng, C. Xu, S.-S. Bao and L.-M. Zheng, *Dalton Trans.*, 2023, **52**, 11913–11921.
4 Q.-C. Luo, Z.-H. Li, J. Lu and Y.-Z. Zheng, *Inorg. Chem. Front.*, 2025, **12**, 3695–3703.
5 B.-K. Ling, M. Chang, Y.-Q. Zhai, J. Deng, M. Kofu, H. Guo, J. Zhao, Z. Fu and Y.-Z. Zheng, *J. Am. Chem. Soc.*, 2025, **147**, 10935–10942.
6 F. Pointillart, K. Bernot, B. Le Guennic and O. Cador, *Chem. Commun.*, 2023, **59**, 8520–8531.
7 P. Kumar Sahu and S. Konar, *Chem. – Eur. J.*, 2024, **30**, e202402439.
8 P. Kumar Sahu, A. Mondal and S. Konar, *Chem. – Eur. J.*, 2023, **29**, e202203664.
9 P. Kumar Sahu, R. Kharel, S. Shome, S. Goswami and S. Konar, *Coord. Chem. Rev.*, 2023, **475**, 214871.
10 A. Gupta, S. Kapurwan, S. Prasad Bera, D. Jyoti Mondal, S. Shome and S. Konar, *Chem. – Asian J.*, 2022, **17**, e202200622.
11 P. K. Sahu, S. Kapurwan and S. Konar, *Chem. Commun.*, 2025, **61**, 6105–6117.
12 A. S. Armenis, A. Mondal, S. R. Giblin, C. P. Raptopoulou, V. Psycharis, D. I. Alexandropoulos, J. Tang, R. A. Layfield and T. C. Stamatatos, *Chem. Commun.*, 2024, **60**, 12730–12733.
13 X.-D. Huang, X.-F. Ma, T. Shang, Y.-Q. Zhang and L.-M. Zheng, *Inorg. Chem.*, 2023, **62**, 1864–1874.
14 W.-J. Xu, Q.-C. Luo, Z.-H. Li, Y.-Q. Zhai and Y.-Z. Zheng, *Adv. Sci.*, 2024, **11**, 2308548.
15 N. El Beyrouti, F. Houard, M. Cordier, E. Trzop, S. Rigaut, B. Le Guennic, K. Bernot and L. Norel, *Chem. Commun.*, 2023, **59**, 5265–5268.
16 N. Jain, G. David, M. Cordier, Y. Suffren, B. L. Guennic, Y. Sarazin and K. Bernot, *ChemistryEurope*, 2025, 202500193.
17 D. A. Gálico and M. Murugesu, *Angew. Chem., Int. Ed.*, 2023, **62**, e202309152.
18 Q. Yang, J. Wu, C. Zhao, X. Ying, D.-M. Zhu, X. Guo, D. Liu, Y.-Q. Zhang and J. Tang, *Chem. Commun.*, 2025, **61**, 8751–8754.
19 C.-Y. Jin, Q. Zhang, J. Tang, P. Cheng and L. Li, *Dalton Trans.*, 2025, **54**, 7718–7725.
20 Y. Wang, Q.-C. Luo and Y.-Z. Zheng, *Angew. Chem., Int. Ed.*, 2024, **63**, e202407016.
21 J. J. Zakrzewski, M. Liberka, J. Wang, S. Chorazy and S.-I. Ohkoshi, *Chem. Rev.*, 2024, **124**, 5930–6050.
22 X.-D. Huang, X.-F. Ma and L.-M. Zheng, *Angew. Chem., Int. Ed.*, 2023, **62**, e202300088.
23 X.-F. Ma, Y. Guo, X.-D. Huang, G.-H. Wen, S.-S. Bao, Y.-Q. Zhang and L.-M. Zheng, *Dalton Trans.*, 2022, **51**, 12026–12030.
24 S. Shome, N. C. Maurya, M. Mukherjee, K. V. Adarsh and S. Konar, *Chem. Commun.*, 2025, **61**, 2337–2340.
25 H. Song, Z.-C. Wu, Y. Chen, N. Yang, Z. Zhang, M. D. Dramićanin and J. Li, *Adv. Opt. Mater.*, 2025, 2500107.
26 À. Tubau, L. Rodríguez, P. Pander, L. Weatherill, F. B. Dias, M. Font-Bardía and R. Vicente, *J. Mater. Chem. C*, 2024, **12**, 8127–8144.
27 V. Vieru, S. Gómez-Coca, E. Ruiz and L. F. Chibotaru, *Angew. Chem., Int. Ed.*, 2024, **63**, e202303146.
28 R. M. Diaz-Rodriguez, D. A. Gálico, D. Chartrand, E. A. Suturina and M. Murugesu, *J. Am. Chem. Soc.*, 2022, **144**, 912–921.
29 M. Tan, F. Li, N. Cao, H. Li, X. Wang, C. Zhang, D. Jaque and G. Chen, *Small*, 2020, **16**, 2004118.
30 D. Errulat, R. Marin, D. A. Gálico, K. L. M. Harriman, A. Pialat, B. Gabidullin, F. Iikawa, O. D. D. Couto, Jr., J. O. Moilanen, E. Hemmer, F. A. Sigoli and M. Murugesu, *ACS Cent. Sci.*, 2019, **5**, 1187–1198.
31 G. Brunet, R. Marin, M.-J. Monk, U. Resch-Genger, D. A. Gálico, F. A. Sigoli, E. A. Suturina, E. Hemmer and M. Murugesu, *Chem. Sci.*, 2019, **10**, 6799–6808.
32 R. Marin, D. A. Gálico, R. Gayfullina, J. O. Moilanen, L. D. Carlos, D. Jaque and M. Murugesu, *J. Mater. Chem. C*, 2022, **10**, 13946–13953.
33 A. A. Kitos, D. A. Gálico, R. Castañeda, J. S. Ovens, M. Murugesu and J. L. Brusso, *Inorg. Chem.*, 2020, **59**, 11061–11070.
34 A. A. Kitos, D. A. Gálico, N. Mavragani, R. Castañeda, J. O. Moilanen, J. L. Brusso and M. Murugesu, *Chem. Commun.*, 2021, **57**, 7818–7821.
35 R. A. S. Ferreira, E. Mamontova, A. M. P. Botas, M. Shestakov, J. Vanacken, V. Moshchalkov, Y. Guari,

L. F. Chibotaru, D. Luneau, P. S. André, J. Larionova, J. Long and L. D. Carlos, *Adv. Opt. Mater.*, 2021, **9**, 2101495.
36 K. Karachousos-Spiliotakopoulos, V. Tangoulis, N. Panagiotou, A. Tasiopoulos, E. Moreno-Pineda, W. Wernsdorfer, M. Schulze, A. M. P. Botas and L. D. Carlos, *Dalton Trans.*, 2022, **51**, 8208–8216.
37 K. Karachousos-Spiliotakopoulos, V. Tangoulis, N. Panagiotou, A. Tasiopoulos, V. Nastopoulos, E. Moreno-Pineda, W. Wernsdorfer, M. Schulze, A. M. P. Botas and L. D. Carlos, *Inorg. Chem.*, 2022, **61**, 18629–18639.
38 K. Kumar, O. Stefanczyk, K. Nakabayashi, K. Imoto, Y. Oki and S.-I. Ohkoshi, *Adv. Opt. Mater.*, 2022, **10**, 2101721.
39 K. Kumar, D. Abe, K. Komori-Orisaku, O. Stefańczyk, K. Nakabayashi, J. R. Shakirova, S. P. Tunik and S.-I. Ohkoshi, *RSC Adv.*, 2019, **9**, 23444–23449.
40 J. Wang, J. J. Zakrzewski, M. Heczko, M. Zychowicz, K. Nakagawa, K. Nakabayashi, B. Sieklucka, S. Chorazy and S.-I. Ohkoshi, *J. Am. Chem. Soc.*, 2020, **142**, 3970–3979.
41 K. Kumar, O. Stefanczyk, S. Chorazy, K. Nakabayashi and S.-I. Ohkoshi, *Adv. Opt. Mater.*, 2022, **10**, 2201675.
42 J. Wang, J. J. Zakrzewski, M. Zychowicz, Y. Xin, H. Tokoro, S. Chorazy and S.-I. Ohkoshi, *Angew. Chem., Int. Ed.*, 2023, **62**, e202306372.
43 S. Zanella, M. Aragon-Alberti, C. D. S. Brite, F. Salles, L. D. Carlos and J. Long, *Angew. Chem., Int. Ed.*, 2023, **62**, e202306970.
44 D. A. Gálico and M. Murugesu, *Angew. Chem., Int. Ed.*, 2025, **64**, e202505806.
45 A. G. Bispo-Jr, *Coord. Chem. Rev.*, 2025, **537**, 216685.
46 J. Liu, Y.-C. Chen, J.-L. Liu, V. Vieru, L. Ungur, J.-H. Jia, L. F. Chibotaru, Y. Lan, W. Wernsdorfer, S. Gao, X.-M. Chen and M.-L. Tong, *J. Am. Chem. Soc.*, 2016, **138**, 5441–5450.
47 Y. Yu, L. Tauxe and B. M. Moskowitz, *Geochem., Geophys., Geosyst.*, 2004, **5**, Q06H11.
48 D. N. Woodruff, R. E. P. Winpenny and R. A. Layfield, *Chem. Rev.*, 2013, **113**, 5110–5148.
49 A. S. Armenis, A. Mondal, S. R. Giblin, D. I. Alexandropoulos, J. Tang, R. A. Layfield and T. C. Stamatatos, *Inorg. Chem. Front.*, 2025, **12**, 1214–1224.
50 M. S. Raju, K. Paillot, I. Breslavetz, G. Novitchi, G. L. J. A. Rikken, C. Train and M. Atzori, *J. Am. Chem. Soc.*, 2024, **146**, 23616–23624.
51 J. Wang, J. J. Zakrzewski, M. Zychowicz, V. Vieru, L. F. Chibotaru, K. Nakabayashi, S. Chorazy and S.-I. Ohkoshi, *Chem. Sci.*, 2021, **12**, 730–741.

